RMetS
Royal Meteorological Society

An analysis of the observed low-level structure of rapidly intensifying and mature hurricane *Earl* (2010)

Michael T. Montgomery,[a]* Jun A. Zhang[b] and Roger K. Smith[c]
[a]*Department of Meteorology, Naval Postgraduate School, Monterey, CA, USA*
[b]*NOAA Hurricane Research Division, Miami, FL, USA*
[c]*Meteorological Institute, Ludwig Maximilians, University of Munich, Germany*

*Correspondence to: M. T. Montgomery, Department of Meteorology, Naval Postgraduate School, Monterey, CA 93943, USA.
E-mail: mtmontgo@nps.edu

We examine dynamic and thermodynamic aspects of Atlantic hurricane *Earl* (2010) during its intensification and mature phases over four days of intensive measurements. During this period, *Earl* underwent an episode of rapid intensification, maturity, secondary eyewall replacement, re-intensification and the early part of its decline. The observations are used to appraise elements of a new model for tropical-cyclone intensification.

The results affirm the conventional (vortex interior) and boundary-layer spin-up mechanisms that form dynamical elements of the azimuthally averaged view of the new intensification model. The average maximum tangential winds beneath the eyewall are found to exceed the gradient wind by between 20 and 60%. The results suggest also that the gradient wind balance approximation in the low-level vortex interior above the strong inflow layer may not be as accurate in the inner-core region of a tropical cyclone during its intensification as has been widely held. An analysis of the low-level thermodynamic structure affirms the radial increase of moist equivalent potential temperature, θ_e, with decreasing radius during the intensification process, a necessary ingredient of the new model for maintaining convective instability in the presence of a warming upper troposphere. An unanticipated finding is the discovery of an unmixed boundary layer in terms of θ_e within several hundred kilometres of the vortex centre. In the inner-core region, this finding is not consistent with the axisymmetric eruption of the boundary layer into the eyewall unless there are non-conservative (eddy) processes acting to modify the entropy of ascending air.

Key Words: hurricanes; typhoons; conventional spin-up mechanism; boundary-layer spin-up mechanism; thermodynamic structure; surface enthalpy fluxes; GRIP

Received 28 February 2013; Revised 6 September 2013; Accepted 16 October 2013; Published online in Wiley Online Library

1. Introduction

Early theories of tropical-cyclone intensification emphasized the role of deep convective clouds, which, in an azimuthally averaged sense, generate radial convergence in the low to mid-troposphere (Charney and Eliassen, 1964; Ooyama, 1964). These authors showed that spin-up was a result of the accompanying import of absolute angular momentum, M, above the frictional boundary layer, where M is materially conserved. Here $M = rv + (1/2)fr^2$, where r denotes radius from storm centre, v denotes azimuthally averaged, storm-relative tangential velocity and f denotes the Coriolis parameter.

Dissatisfied by thermodynamical aspects of the foregoing studies, Ooyama formulated a highly simplified three-layer slab model with an entraining-plume representation of deep convection on the vortex scale and of sensible and latent heat fluxes from the underlying ocean (Ooyama, 1969). As in the earlier models, the spin-up was associated with the convectively induced import of M, but that spin-up required a supply of latent heat energy from the ocean to maintain the (parametrized) deep convection. We will refer to the convectively induced import of M above the boundary layer, in conjunction with the supply of moisture from the underlying ocean surface, as the conventional intensification model (Ooyama, 1969, 1982; Willoughby, 1988, 1995).

A seemingly different model for spin-up was proposed by Emanuel (1997) which focussed more on the thermodynamic controls on the intensification process but, as noted by Montgomery and Smith (2013), the dynamical mechanism for spin-up appears to be again the radial import of M above the

Report Documentation Page

Form Approved
OMB No. 0704-0188

1. REPORT DATE	2. REPORT TYPE	3. DATES COVERED
2014		**00-00-2014 to 00-00-2014**

4. TITLE AND SUBTITLE	5a. CONTRACT NUMBER
An Analysis of the Observed Low-level Structure of Rapidly Intensifying and Mature Hurricane Earl (2010)	5b. GRANT NUMBER
	5c. PROGRAM ELEMENT NUMBER
6. AUTHOR(S)	5d. PROJECT NUMBER
	5e. TASK NUMBER
	5f. WORK UNIT NUMBER
7. PERFORMING ORGANIZATION NAME(S) AND ADDRESS(ES) **Naval Postgraduate School,Department of Meteorology,Monterey,CA,93943**	8. PERFORMING ORGANIZATION REPORT NUMBER
9. SPONSORING/MONITORING AGENCY NAME(S) AND ADDRESS(ES)	10. SPONSOR/MONITOR'S ACRONYM(S)
	11. SPONSOR/MONITOR'S REPORT NUMBER(S)

12. DISTRIBUTION/AVAILABILITY STATEMENT
Approved for public release; distribution unlimited

13. SUPPLEMENTARY NOTES

14. ABSTRACT

15. SUBJECT TERMS

16. SECURITY CLASSIFICATION OF:			17. LIMITATION OF ABSTRACT	18. NUMBER OF PAGES	19a. NAME OF RESPONSIBLE PERSON
a. REPORT	b. ABSTRACT	c. THIS PAGE			
unclassified	**unclassified**	**unclassified**	**Same as Report (SAR)**	**15**	

frictional boundary layer by deep convection. An appraisal of these early paradigms for tropical cyclone intensification, all of which are axisymmetric, is given by Montgomery and Smith (2013).

A new paradigm for tropical-cyclone intensification has been expounded in a series of recent articles (Nguyen *et al.*, 2008; Montgomery *et al.*, 2009; Smith *et al.*, 2009, Bui *et al.*, 2009) and summarized by Montgomery and Smith (2013). This paradigm was distilled from the results of the foregoing studies using observations and high-resolution, three-dimensional, numerical model simulations that represent deep convection explicitly and recognize the role of rotating deep convection in the spin-up process. Analyses of azimuthally averaged fields in the foregoing simulations led to a revised view of spin-up that includes the conventional intensification mechanism, but emphasizes the important *dynamical role* of the boundary layer*. In fact, Smith *et al.* (2009) showed that the spin-up of the maximum tangential winds takes place *within* the frictional boundary layer, although the spin-up of the winds above the boundary layer (which are widely held to be in approximate gradient wind balance) is necessary as well. (A similar result was noted by Zhang *et al.* (2001) in a simulation of hurricane *Andrew* (1992), but they did not appear to recognize the generality of their result.) As in the earlier paradigms, the spin-up of the bulk vortex above the boundary layer occurs through the conventional mechanism, as discussed above.

The boundary-layer spin-up mechanism may seem counter-intuitive to those who have studied boundary layers only in the context of non-rotating flows, where friction reduces the flow near the boundary. The mechanism is possible because the inward displacement of air parcels is much larger in the boundary layer than above, a consequence of the frictional disruption of gradient wind balance which holds approximately above the boundary layer. This disruption leads to a net inward force in the boundary layer. Since the azimuthal mean tangential wind speed $v = M/r - (1/2)fr$, the possibility arises that the loss of M to the surface following an air parcel may be more than offset by a large inward displacement of the air parcel, so that the tangential wind increases and eventually becomes larger than that above the boundary layer. In high-resolution model simulations, the process is exemplified by time–height cross-sections of the azimuthally averaged M surfaces, which tilt inwards with height within the boundary layer and outwards with height above, with a 'nose' at the top of the boundary layer. While there have been observations of such nose-like structures in a mature hurricane (e.g. Bell and Montgomery, 2008), to our knowledge the evolution of the M surfaces during intensification has not been reported for an intensifying tropical cyclone.

While the boundary-layer spin-up mechanism presumes an increasing gradient wind and radial pressure gradient at the top of the boundary layer in association with the conventional mechanism, it contributes also to the spin-up of the bulk vortex through the lofting of the enhanced tangential momentum into the bulk vortex and a corresponding adjustment of the bulk wind and mass fields toward the higher winds from the boundary layer.

In a nutshell, on the system-scale, the new spin-up paradigm has two dynamical components. The first is the conventional spin-up mechanism, i.e. convectively induced inflowing rings of air in the lower troposphere which approximately materially conserve their M. The second component comprises the boundary-layer spin-up mechanism summarized in the foregoing discussion. A related and essential ingredient of the new spin-up paradigm is the maintenance of convective instability in the inner-core region of the vortex, as discussed above.

Although the focus of the present study is on the low-level structure of both the intensification and mature phases of a hurricane, some aspects of Emanuel's steady-state hurricane model (Emanuel, 1986, henceforth E86) still provide a useful context for interpreting observations of an intensifying storm. An important feature of this model is the assumption that, as air parcels ascend along the eyewall, they conserve their absolute angular momentum, M, and saturation pseudo-equivalent potential temperature, θ_e^*, so that M and θ_e^* surfaces are congruent. In addition, the theory assumes explicitly that the tangential flow above the boundary layer is in gradient wind balance. An important constraint in the model is the rate at which M and θ_e^* vary with radius in the boundary layer inside the radius of maximum tangential wind speed (r_m), which E86 assumes to be located at the outer edge of the eyewall (Figure 1 of E86). A brief summary of the model formulation is contained in section 2 of Smith *et al.* (2008). While the model has undergone a number of reincarnations over the years (Emanuel, 1988, 1995, 2004, 2012; Bister and Emanuel, 1998, 2002; Emanuel and Rotunno, 2011), the foregoing aspects have remained unchanged.

An important feature of the E86 model is the increase in θ_e^* with diminishing radius in the vicinity of the eyewall updraught. Such a feature had been documented earlier from observational analyses (Hawkins and Imbembo, 1976) and has been confirmed by more recent work (Montgomery *et al.*, 2006; Marks *et al.*, 2008; Bell and Montgomery, 2008). Since the virtual temperature, θ_v, in cloud increases monotonically with θ_e^*, θ_v must increase also with decreasing radius at a given pressure level, consistent with the warm core structure of the vortex. Because ascending air parcels move to larger radii, the M and θ_e^* surfaces flare outwards with height. As these air parcels move outwards conserving M, they spin more slowly about the rotation axis of the storm. This fact, together with the positive radial gradient of M, explains the observed decrease of the tangential wind speed with height, consistent with the thermal wind equation (E86). As discussed by Montgomery and Smith (2013), in the new intensification paradigm, only modest surface moisture fluxes are required from the underlying ocean, which give rise to an increase of boundary layer θ_e with decreasing radius. The θ_e increase is needed to help maintain a degree of convective instability of the inner-core region in the presence of a developing warm core aloft. This increase does not necessarily require an evaporative–wind feedback process as hypothesized by Emanuel *et al.* (1994) and Emanuel (2003). In fact, Montgomery *et al.* (2009) have shown that this evaporative–wind feedback mechanism is neither essential nor the dominant pathway for tropical cyclone spin-up.

Observational support of the second spin-up mechanism for tropical cyclone intensification was presented by Sanger (2011) and Sanger *et al.* (~~2013~~), who examined the azimuthally averaged boundary-layer structure during the intensification of typhoon *Jangmi*, which was observed as part of the Tropical Cyclone Structure 2008 (TCS08) experiment (Elsberry and Harr, 2008). An even more detailed dataset for testing this spin-up mechanism and the new intensification paradigm was obtained in hurricane *Earl* (2010) during four days of intensive measurements based on airborne dropwindsondes released from the upper troposphere during the collaborative National Aeronautics and Space Administration (NASA), Genesis and Rapid Intensification Processes (GRIP) and the National Oceanic and Atmospheric Administration (NOAA) Intensity and Foreasting Experiment (IFEX). Here we examine the kinematic, dynamic and thermodynamic structure of this Atlantic hurricane during its intensification and mature phases. During the extensive observation period, *Earl* underwent one episode

*In this work, we use the term boundary layer to describe the shallow layer of strong inflow near the sea surface that is typically 500 m to 1 km deep and which arises largely because of the frictional disruption of gradient wind balance near the surface (e.g. Figure 6 of Smith *et al.*, 2009). This dynamical definition is uncontroversial in the outer regions of a tropical cyclone vortex, where there is subsidence into the boundary layer, but it has limitations in the inner-core region where boundary-layer air is being lofted into the eyewall clouds. In the latter region, conventional boundary-layer theory breaks down. For one thing, vertical perturbation pressure gradients may not be ignored there. The flow in this region is akin to that of separation in aerodynamic boundary layers. Smith and Montgomery (2010) provide further discussion on hurricane boundary layers. Here, we acknowledge this limitation, but adopt the layer of relatively strong inflow as the boundary layer.

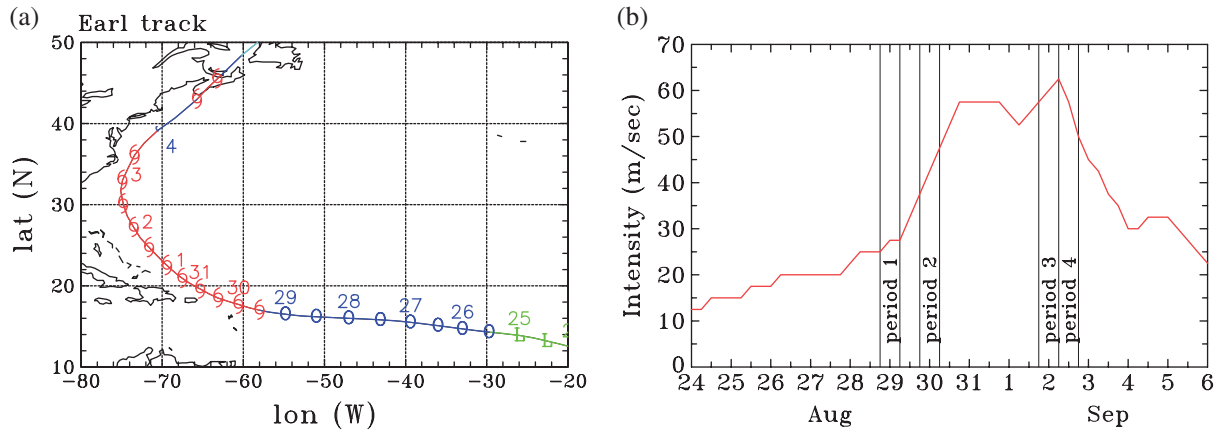

Figure 1. (a) Best-track positions, and (b) intensity for hurricane *Earl*, 25 August–4 September 2010, based on 'best track' data from the National Hurricane Center archive. The vertical lines in (b) delineate the four periods of flight reconnaissance referred to in the text.

of rapid intensification and the measurements afford a unique opportunity to assess several aspects of the new paradigm of tropical cyclone intensification. They afford also the possibility of extending the analysis of Smith and Montgomery (2013a) to quantify the changes in the radial distribution of boundary-layer θ_e as the storm intensifies. Like the study by Sanger *et al.* (~~2013~~), we will adopt a system-scale viewpoint of the intensification process and use a composite methodology to construct an approximate azimuthally averaged picture of the evolving vortex. An analysis of the asymmetric processes is beyond the scope of this study.

The article is organized as follows. In section 2, we give a brief summary of hurricane *Earl*, focussing largely on the period from rapid intensification to maturity. In section 3, we summarize the data quality and analysis methodology employed. Sections 4 and 5 present the analysis of the observational data. Section 6 presents a summary of the main findings and discusses some implications of the results.

2. Hurricane *Earl* and data collected

Hurricane *Earl* originated from a strong tropical wave that left the west coast of Africa on 23 August 2010. The US National Hurricane Center (NHC) 'best track' chart of *Earl*'s path is given in Figure 1(a), with the time series of its intensity shown in Figure 1(b). The following description is based on the storm summary produced by the NHC.

Strong subtropical ridging over the eastern Atlantic steered *Earl* westwards to westnorthwestwards at a speed of between 7.5 and 10 m s^{-1} for the next few days. At the same time, the tropical storm strengthened gradually over a sea surface temperature of 28–29 °C and in an environment of light to moderate vertical shear. Data from an Air Force Reserve reconnaissance aircraft indicated that *Earl* became a hurricane by 1200 UTC on 29 August, when centred about 220 n. miles (400 km) east of the northern Leeward Islands. Around that time, *Earl* neared a weakness in the subtropical ridge associated with hurricane *Danielle* to its west, and it slowed and gradually turned northwestwards while undergoing rapid intensification. *Earl* strengthened to a category 3 hurricane about 12 h later, when it was located very near the northern Leeward Islands. Data from both NOAA and Air Force hurricane hunter aircraft, along with satellite imagery, indicate that *Earl* intensified by 40 kt over 24 h, becoming a category 4 hurricane by 1800 UTC on 30 August.

Figure 2 shows a composite reflectivity from the lower-fuselage (5 cm) radar on the NOAA P3 aircraft during four missions into the intensifying storm. The reflectivity image centred at 2250 UTC on 28 August shows a cyclonically curved band of high reflectivity (exceeding 40 dBZ) that extended from the southwest to the east of the centre. At this time the developing eye, which was marked in the centre by very low reflectivity values (below 15 dBZ), had an approximately oval shape with diameter of 60 km in the east–west direction and 80 km in the north–south direction. By 1040 UTC on 29 August, the eye boundary had become more circular and the reflectivity pattern became a little more symmetric about the centre. During the next 12 h the eye region contracted and remained approximately symmetric with a final diameter of approximately 50 km at 2200 UTC on 29 August. Again, the reflectivity pattern became asymmetric with two prominent reflectivity bands wrapping cyclonically inwards on the southeastern side of the centre. It was during this interval that the vortex intensified rapidly (cf. Figure 1(b)). After another 12 h by 1230 UTC on 30 August the eye had contracted further and was almost surrounded by a narrow region of high reflectivity, characterizing a developing eyewall. The reflectivity of this eyewall was most extensive in the southeast sector. The bands of high reflectivity in the previous image had disappeared. A moat of low reflectivity was apparent mainly on the western and southwestern sides of the eye. The intensity at this time was approximately 55 m s^{-1}.

Subsequently, *Earl* began a concentric eyewall replacement cycle that was well observed in both the San Juan Doppler radar and aircraft flight-level wind data. This cycle halted the intensification process and *Earl* remained a 115 kt (59 m s^{-1}) hurricane for the next 24 h. Southwesterly shear increased late on 31 August, which resulted in *Earl* weakening back to a category 3 hurricane by 0000 UTC on 1 September. *Earl* weakened a little more during the morning hours of 1 September, but by that afternoon the eye became more distinct and deep convective activity increased and gained symmetry, presumably due to a decrease in vertical shear. *Earl* re-intensified to category 4 strength by 1800 UTC on 1 September and reached its peak intensity of 63 m s^{-1} 12 h later, when it was located about 380 n. miles (700 km) southeast of Wilmington, North Carolina. An infrared satellite image of *Earl* near its peak intensity is shown in Figure 3. *Earl* then rapidly weakened as it turned northwards, falling below major hurricane status by 0000 UTC on 3 September.

3. Data quality and analysis methodology

Hurricane *Earl* was extensively sampled by multiple research and reconnaissance aircraft from NOAA, NASA and the US Air Force prior to, during, and at the end of the period of rapid intensification, with less than 12 h between sampling times for the inner core and less than 24 h for the environment. This represents one of most intensively sampled lifecycles of rapid intensification ever. In our analyses, we use the Global Positioning System (GPS) dropwindsonde (henceforth dropsonde) data collected in hurricane *Earl* between 28 August and 2 September 2010. As an example, Figure 4 shows the dropsonde data coverage relative to the storm centre obtained from four different research aircraft. The position of each dropsonde corresponds to the position when

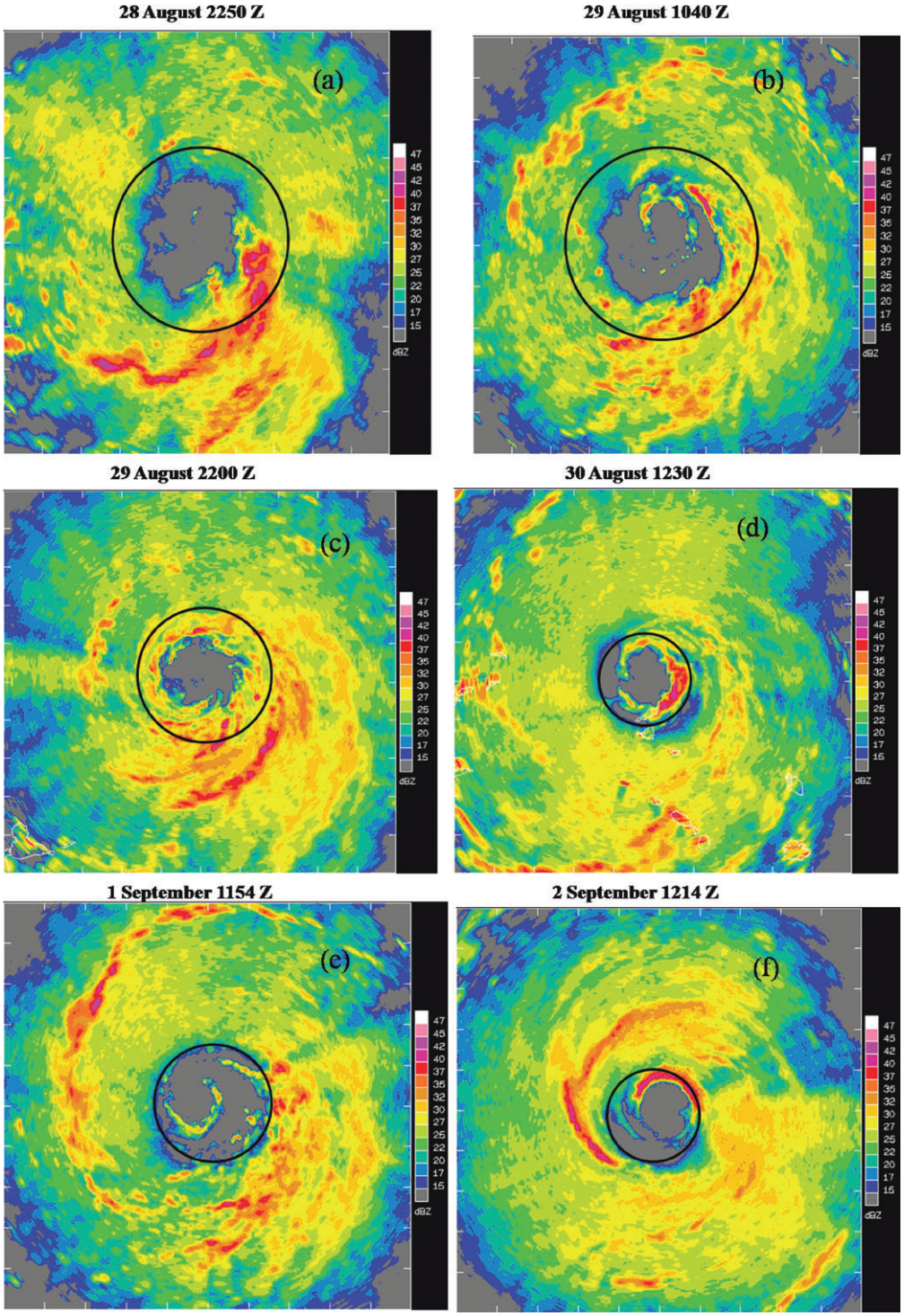

Figure 2. The reflectivity field as viewed by the lower fuselage radar of the NOAA WP-3D aircraft at (a) 2250 UTC on 28 August, (b) 1040 UTC on 29 August, (c) 2200 UTC on 29 August, (d) 1230 UTC on 30 August, (e) 1154 UTC on 1 September, and (f) 1214 UTC on 2 September. (Z is same as UTC) All six panels are 360 km × 360 km. The colour bar shows values in ranges of dBZ. The bold circles denote the radius of maximum azimuthally averaged, storm-relative tangential wind deduced from the Doppler radar data.

the dropsonde was first released, but analyses in the forthcoming section use the instantaneous position of the dropsonde at a particular height. We group the data into 12 h windows to increase the sample size and focus on four periods, two during the period of rapid intensification (1800 UTC 28 August to 0600 UTC 29 August (period 1), and 1800 UTC 29 August to 0600 UTC 30 August (period 2)) and two in which *Earl* had reached a quasi-steady state (1800 UTC 1 September to 0600 UTC 2 September (period 3), and 0600 UTC 2 September to 1800 UTC 2 September (period 4)). These four periods are indicated in Figure 1(b). Table 1 presents an overall summary of the dropsonde analysis periods, eyewall composite region, number of dropsondes used to form the composite, and the total number dropsondes within 250 km radius.

All the dropsonde data were quality controlled using the ASPEN software, which is based on the EDITSONDE software developed by the Hurricane Research Division (Franklin *et al.*, 2003). A standard 10 s filter was used to smooth turbulent noise and switching between GPS satellites, as in Powell *et al.* (2003). A more detailed description of the observational instruments inside the dropwindsonde can be found in Hock and Franklin (1999). The accuracy of the horizontal wind speed measurements is 2.0 m s^{-1} and < 0.5 m s^{-1} for the vertical winds, with approximately 0.2 m s^{-1} precision. The storm centre was determined from the flight-level data using the Willoughby and Chelmow (1982) method along with the best-track data record.

The radial and tangential components are computed relative to the instantaneous storm centre. We averaged the data located

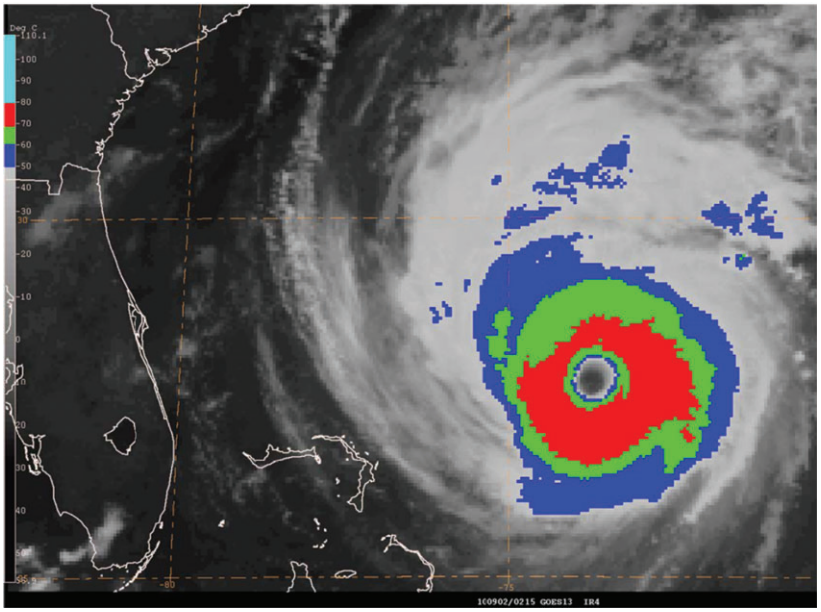

Figure 3. An infrared satellite image at 0215 UTC on 2 August 2010 of hurricane *Earl* near its peak intensity.

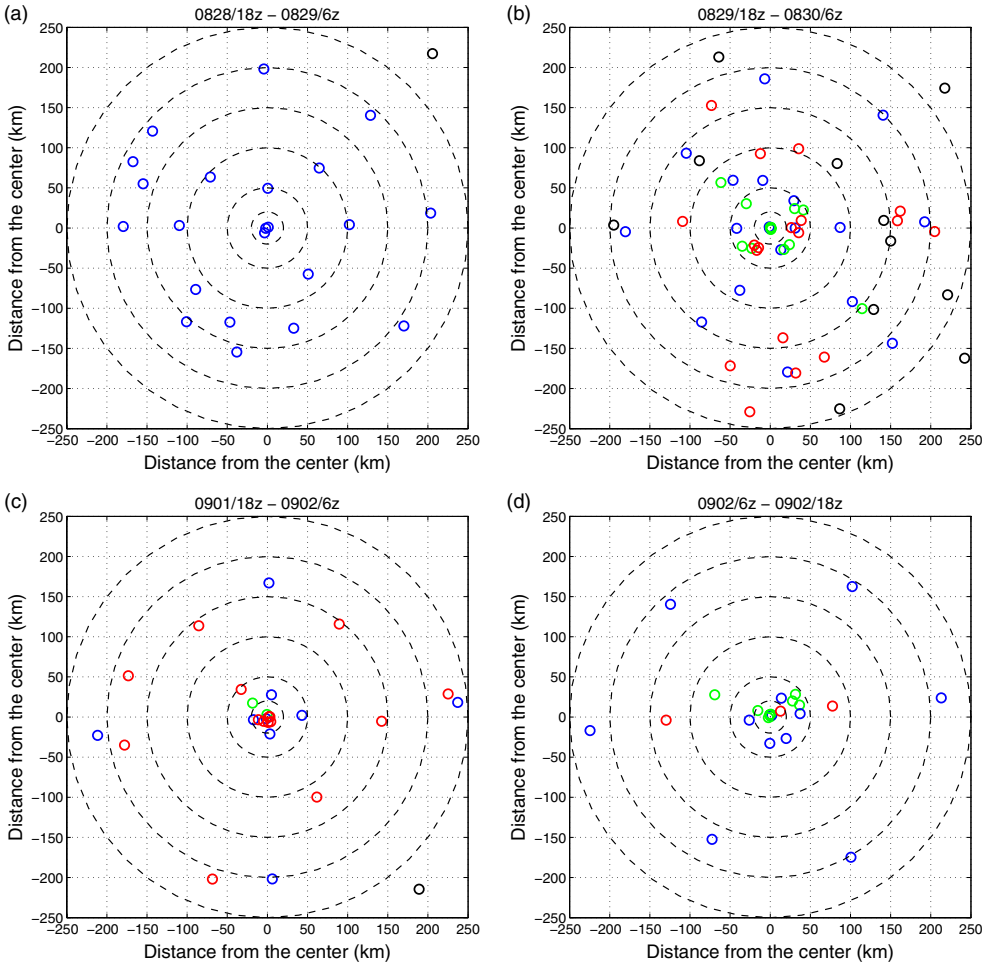

Figure 4. Storm-centred dropsonde distribution over the five days of monitoring of *Earl* by four different research aircraft. Each circle represents the location and type of aircraft from which dropsondes were released: blue WP-3D, red DC-8, green C-130, and black G-IV aircraft. For simplicity, the storm-relative horizontal trajectory of each dropsonde after release time is not shown. [Correction added ~~12~~ 17 September 2014 after original online publication: in Figure 4(b) the period has been corrected to '18Z Aug 29 - 6 Z Aug 30'.]

Table 1. Periods of interest for sonde analyses. See text for details.

Period	Start time (UTC)	End time (UTC)	Eyewall range (km)	Number of sondes in the eyewall region	Total number of sondes within 250 km
1	1800 28 Aug	0600 29 Aug	95–105	3	20
2	1800 29 Aug	0600 30 Aug	35–45	4	32
3	1800 1 Sep	0600 2 Sep	20–30	3	16
4	0600 2 Sep	1800 2 Sep	25–35	3	18

Table 2. Summary of P3 radar data corresponding to Figures 2, 5 and 6. See text for further details.

Flight ID	Start time (radar) (UTC)	End time (radar) (UTC)	RMW (km)	Maximum azimuthally-averaged M at RMW ($m^2 s^{-1}$)	Maximum azimuthally-averaged V_t at RMW ($m\,s^{-1}$)
100828I	2132	0131*	65	1.66×10^6	23.8
100829H	0922	1318	101	2.82×10^6	25.6
100829I	2057	0038*	49	1.80×10^6	34.9
100830H	1110	1341	35	0.82×10^6	36.2
100901H	1056	1217	45	2.46×10^6	52.1
100902H	0935	1213	31	1.70×10^6	55.6

*next day.

within the eyewall region, and found the height of the maximum mean tangential wind speed. To calculate the gradient wind at this height, first we fitted the pressure data with a quadratic polynomial in a least-squares sense as a function of radius from the storm centre. Next, we calculated the gradient wind by solving the quadratic gradient wind equation for tangential velocity using the inferred radial pressure gradient force (Eq. (1) below). Then, using this methodology, the radial profile of the mean gradient wind can then be compared with the local tangential wind speed at the same level (e.g. Figure 11 later).

4. Doppler-radar analysis and results thereof

4.1. The radar data

The tail Doppler radar data from NOAA's WP-3D aircraft are used to construct storm-centred $r-z$ plots of M for each flight. Such plots are then used to assess the first component of the new intensification paradigm of Montgomery and Smith (2013), in which the conventional intensification mechanism for the system-scale circulation discussed in the Introduction is an important element. Table 2 presents a summary of the radar data collected, including specific flight identification (ID), radar-derived radius of maximum tangential wind (RMW), azimuthally-averaged M and V_t at the RMW.

The data were processed as follows. An automated quality control process was applied before the data analysis (Gamache, 2012). The fore/aft scanning technique was used to create dual-Doppler measurements from a single radial penetration (e.g. Reasor *et al.*, 2009). The Doppler radar projection equations and anelastic mass continuity equation were solved at the same time to derive the three-dimensional wind field via least-squares minimization (Gamache, 1997). The quality-controlled Doppler radials extended from the surface to 20 km with horizontal and vertical grid spacings of 2 km and 0.5 km, respectively. For technical reasons, the vortex centre for the radar analysis was defined using a modified version of the centre-finding method of Marks *et al.* (1992), as detailed by Reasor and Eastin (2012). This centre was very close (within a few km) to the centre determined by the Willoughby and Chelmow (1982) method mentioned above and was used for the dropsonde analysis in the next section.

To determine the distribution of azimuthally averaged M, analyses from individual radial penetrations during each flight were merged. The purpose for merging radar swaths is to create the most complete azimuthal coverage of the core region out to the largest radii. A detailed description of the methodology used for merging the swaths and its limitations is given by Reasor *et al.* (2013). The radar data were observed mainly above 500 m, so most of the data are above the boundary layer.

4.2. Spin-up above the boundary layer

Figure 5 shows the evolution of M surfaces as calculated from the merged Doppler radar data for each flight. Note that, in calculating M, we use a constant f for each flight. The value of f is calculated using the averaged latitude of the moving storm centre for each flight. As the storm moves during the period of eyewall penetrations, we have assumed that structural features of interest are quasi-steady over the observation period. Because the latitude change in the storm centre is small ($< 0.6^\circ$) during the period of eyewall penetrations for each flight, the change in f associated with the moving storm is small ($< 3\%$), implying a negligible change of the M field over the Doppler radar domain shown. It is evident from the figure that M increases with radius at each level during *Earl*'s intensification, implying that the vortex is centrifugally (or inertially) stable (e.g. Shapiro and Montgomery, 1993; Franklin *et al.*, 1993), and that the mean radial inflow can carry air with high M towards the centre to spin up the tangential wind field there. We see also that, indeed, over the period of observations, the M surfaces do move radially inwards. Moreover, the signature of the strengthening boundary-layer inflow is evident by the increase in the upward-outward tilt of the M surfaces in the lower troposphere as these surfaces move inwards. The solid black curves are chosen to highlight a few M surfaces during the rapid intensification phase of the vortex. As an example, in the top-left panel of the curve in Figure 5 (0828I, corresponding to 28 August), two particular M surfaces are identified. The innermost M surface begins near 40 km radius (the edge of the inner Doppler radar data region on this day) and slopes upwards to 10 km height and outwards to 100 km radius. In subsequent panels, this surface becomes more upright and moves inwards to near 25 km radius, where the eyewall has developed and the Doppler radar data are adequate to apply the analysis methodology. At outer radii, a qualitatively similar evolution is observed. The second M surface highlighted in the top-left panel of Figure 5 is seen initially near 140 km radius and during the next 48 h extends vertically and moves inwards to approximately 70 km radius on 30 August (panel 0830H). A similar behaviour is found with the third M surface which enters the domain by 30 August near 125 km (panel 0830I). Over the next three days, this third M surface moves inwards approximately 20 km and extends vertically. In summary, the M surfaces are found to be moving inwards during the period of observations. Although there is some tendency of the M surfaces to bow inwards near 2 km altitude outside of the RMW, we are cautious of attributing much significance to this feature on account of the difficulty of extracting Doppler data at low altitudes.

5. Dropwindsonde analysis and results

5.1. Spin-up in the boundary layer

To assess the boundary-layer spin-up mechanism, we study next the boundary-layer structure using the dropsonde data with a focus on below 2 km altitude in the vicinity of the high wind region of the vortex. Figure 6 shows an example of the dropwindsonde wind data at a level of 1 km obtained during period 1, an interval sampling the rapid intensification period (cf. Figure 1(b)). The Doppler radar-derived wind field (described in the foregoing section) are shown at the same level and time period. The figure broadly supports the assumption that the horizontal wind field in the high-wind region possesses a fair degree of

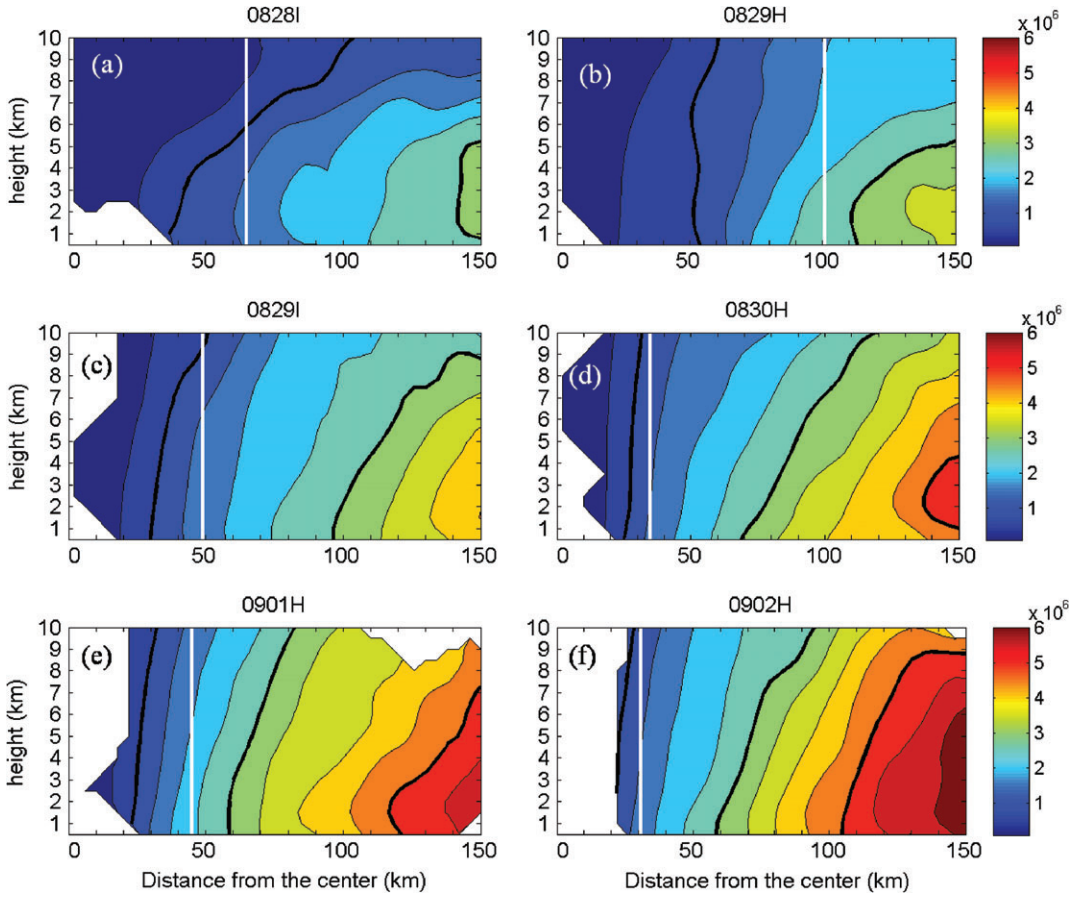

Figure 5. Evolution of absolute angular momentum, M, azimuthally averaged about the storm centre. These M data are from Doppler radar and dropwindsondes, as discussed in section 4. The panels show only the deep tropospheric data above 500 m altitude. The radius of maximum azimuthally averaged tangential velocity at 2 km altitude is indicated by the white vertical line in each panel, and the time for each analysis period is detailed in Table 2.

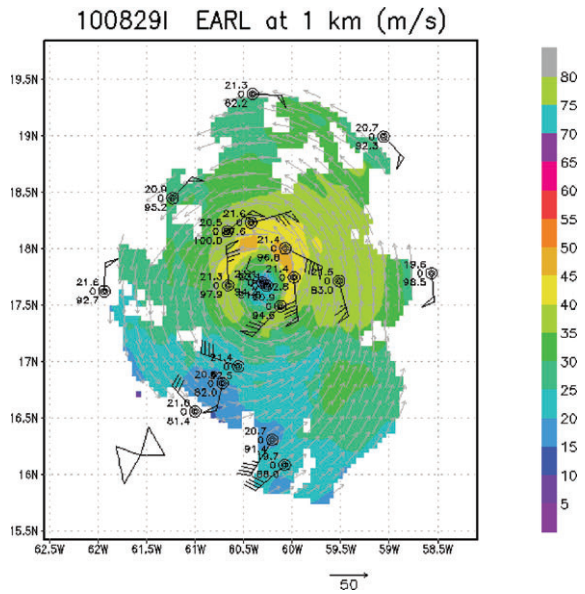

Figure 6. Doppler radar-derived wind vectors for hurricane *Earl* on 29 August (period 1) at a height of 1 km, with speeds colour coded according to the scale on the right. The wind barbs from the dropwindsonde soundings at this level are superimposed. Standard meteorological convention used in displaying dropwindsonde data. (Winds in knots (triangle means 50 knots and flat bar means 10 knots), temperature (in degrees Celsius) and relative humidity (in %)).

symmetry during this period. Similar figures during the other periods have been constructed (not shown) and together they imply that the composite methodology employed herein should provide a meaningful estimate of the azimuthally averaged vortex structure.

Figures 7–10 display the individual and composite vertical profiles of storm-relative tangential (V_t) and radial (V_r) wind speeds in the eyewall region for the four periods of interest, respectively. The eyewall region, and the associated RMW, is determined from the radar data as described in the foregoing subsection. In these figures, individual dropsondes within 5 km of the RMW are shown in colour while the thick black line is the arithmetical-mean vertical profile of the dropsondes. The full 10 m vertical resolution of dropsondes is used here to plot the profiles shown.

Aside from the first set of vertical profiles before rapid intensification has commenced (Figure 7), the averaged profiles indicate that the maximum tangential wind speed occurs persistently well within the vortex boundary layer as defined by the layer of strong inflow (Smith *et al.*, 2009; Zhang *et al.*, 2009, 2011). For example, Figure 8 shows that between 1800 UTC on 29 August and 0600 UTC on 30 August, the maximum composite tangential wind occurs at a height of 400 m, where the mean inflow magnitude exceeds 15 m s^{-1}. Similarly, between 1800 UTC on 1 September and 0600 UTC on 2 September, the maximum composite tangential wind occurs at 500 m and the mean inflow exceeds 30 m s^{-1}! Between 6000 and 1800 UTC on 2 September, the composite tangential wind profile shows some weakening in intensity relative to the previous period, but the maximum tangential wind speed occurs at approximately 750 m where the mean inflow magnitude is still quite significant, 25 m s^{-1}. As discussed in earlier and recent work (Willoughby, 1995; Smith *et al.*, 2009; Bui *et al.*, 2009; Montgomery and Smith, 2013), this layer of strong inflow is driven primarily by the net effective radial pressure gradient brought about by surface friction.

The dropsonde data have the advantage of measuring boundary-layer structure with reasonably high vertical resolution ($\sim$ 10 m). For a well-developed storm such as *Earl*, it is reasonable to assume that the pressure field in the boundary layer is to a first approximation axisymmetric. Then we can estimate the radial profile of pressure at each height by fitting a curve to the pressure observations at each drop location. Using this pressure profile, we

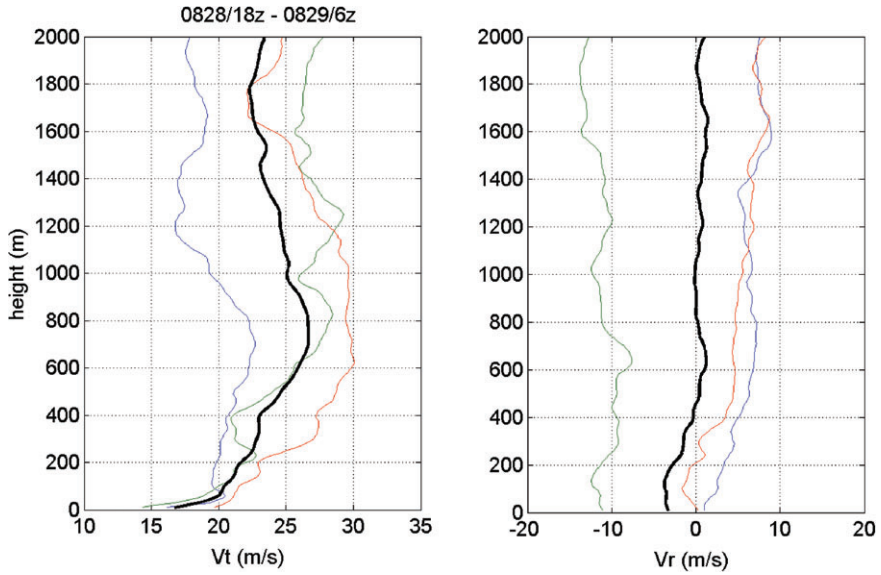

Figure 7. Vertical profiles of storm-relative tangential (V_t) and radial (V_r) wind composites and deviations therefrom in the eyewall region of the vortex during period 1: 1800 UTC on 28 August to 0600 UTC on 29 August. The eyewall region is defined as the region within 5 km from the RMW deduced using the Dopper radar data. Curves for the same sounding have the same colour. Dark solid curves represent the arithmetic average of dropsonde data within the eyewall region. Maximum V_t is generally located well within the boundary layer, while the maximum V_r is often very close to the surface. The average heights of the maximum tangential wind and maximum inflow during this time are 700 and 180 m, respectively (Table 1).

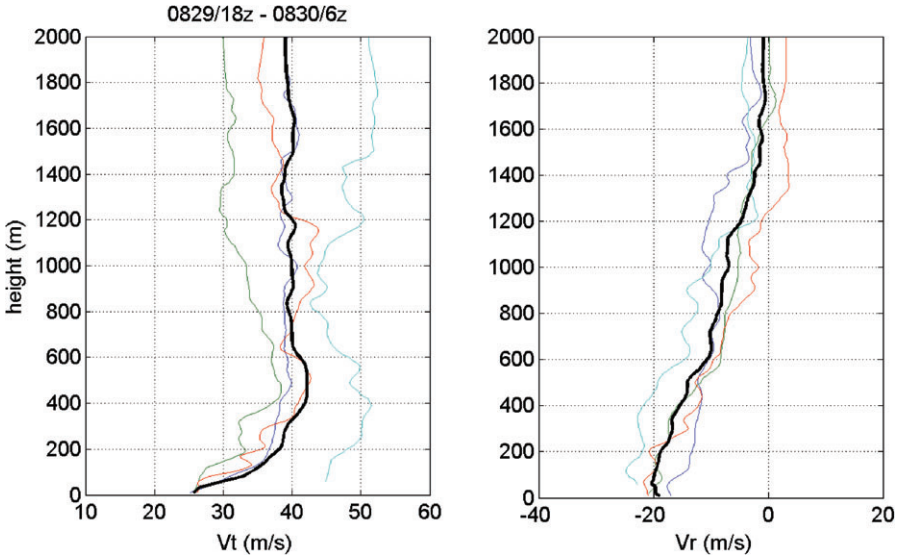

Figure 8. Vertical profiles of storm-relative tangential (V_t) and radial (V_r) wind composites and deviations therefrom in the eyewall region of the vortex during period 2: 1800 UTC 29 August to 0600 UTC 30 August. The eyewall region is defined as the region within 10 km from the RMW deduced using the Dopper radar data. Curves for the same sounding have the same colour. Dark solid curves represent the arithmetic average of dropsonde data within the eyewall region. Maximum V_t is generally located well within the boundary layer, while the maximum V_r is often very close to the surface. The average heights of the maximum tangential wind and maximum inflow during this time are 570 m and 50 m, respectively, while the average height of the inflow layer is 1500 m (Table 1).

may calculate the gradient wind at each analysis height, following the method of Kepert (2006a,b), Bell and Montgomery (2008) and Sanger *et al.* (~~2013~~). Gradient wind balance is defined as a balance between the radial pressure gradient force per unit mass and the sum of centrifugal and Coriolis forces:

$$\frac{1}{\rho}\frac{\partial p}{\partial r} = \frac{V_g^2}{r} + fV_g\,, \tag{1}$$

where V_g is the gradient wind. The gradient wind is obtained by solving the quadratic equation for V_g using the calculated radial pressure gradient as long as the radial pressure gradient remains positive.

Figure 11 shows the results for the gradient wind calculations for the four periods at the height of the maximum tangential wind speed. The left panels show the observed pressure from individual sondes (blue circles) as a function of radius. Shown also are the best fit to the pressure data (red curve) in a quadratic polynomial form using a least-square regression method. The right panels show the observed tangential wind corresponding with each pressure observation. For comparison, the gradient wind is presented as a function of radius also (green curve). The red square in each right panel indicates the averaged value of V_t for the eyewall region. In this region for all periods, the average V_t is significantly higher than the corresponding gradient wind. Specifically, this average wind exceeds the gradient wind by 20% during period 1, 43% during period 2, 60% during period 3, and 32% during period 4. These calculations suggest that, during both the rapid intensification and quasi-steady periods, the boundary-layer flow is significantly supergradient at the height of the maximum tangential wind speed. In contrast to the unbalanced state of affairs in the inner-core boundary layer, Figure 11 shows that, at outer radii, the tangential winds are on average much closer to the gradient wind than at inner radii. At these radii, the radial advection of M is considerably weaker and the boundary layer is more akin to that of a classical Ekman layer.

During spin-up and maturity, the maximum tangential winds occur without exception within the layer of strong boundary-layer

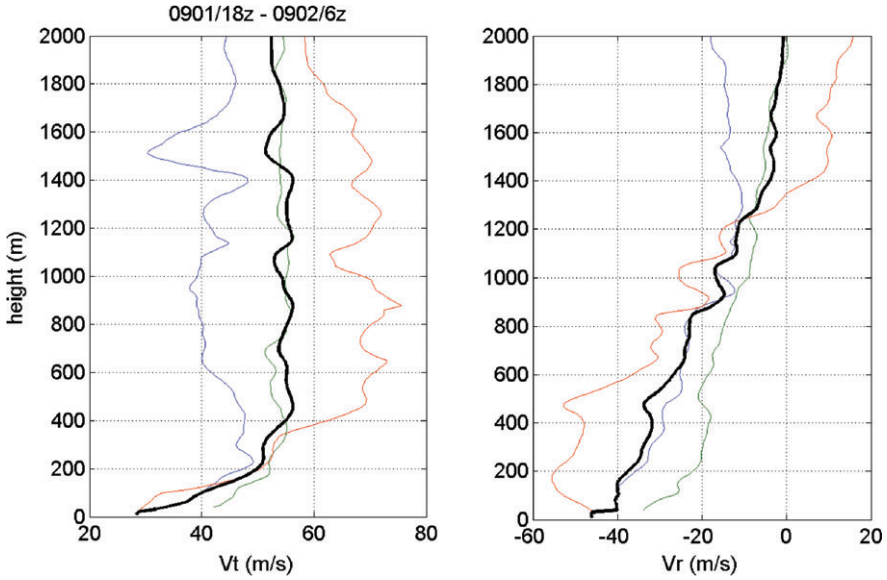

Figure 9. Vertical profiles of storm-relative tangential (V_t) and radial (V_r) wind composites and deviations therefrom in the eyewall region of the vortex during period 3: 1800 UTC on 1 September to 0700 UTC on 2 September. The eyewall region is defined as the region within 10 km from the RMW deduced using the Doppler radar data. Curves for the same sounding have the same colour. Dark solid curves represent the arithmetic average of dropsonde data within the eyewall region. Maximum V_t is generally located well within the boundary layer, while the maximum V_r is often very close to the surface. The average heights of the maximum tangential wind and maximum inflow during this time are 450 m and 50 m, respectively, while the average height of the inflow layer is 1500 m (Table 1).

inflow ($<$ 1 km depth). The tangential winds near the radius of maximum wind in the boundary layer are persistently and significantly supergradient. For brevity, we have shown this feature only at the height of maximum tangential wind, but supporting analyses confirm this tendency throughout much of the boundary layer, except very near the surface where the tangential winds become subgradient. The average maximum tangential wind speeds beneath the eyewall exceed the gradient wind by between 20 and 60%, with the largest excess occurring during the re-intensification period following the eyewall replacement on 2 September. As an indication of the inaccuracy of the gradient wind for characterizing the structure of the vortex in the boundary layer, the radius of the gradient wind maximum is up to three times the radius of the maximum observed tangential wind speed.

In the foregoing calculations, there is a potential issue regarding the apparent scatter of the tangential wind data relative to the computed gradient wind. To address this concern, we recomputed all of the gradient wind calculations for the boundary-layer region using a layer-average of the tangential winds over the layer between 400 and 1000 m, and computed the gradient wind using the dropsonde pressure field at the mid-point of this layer (i.e. 700 m altitude). The results (not shown) corroborate the previous findings. For the case of period 1 (early intensification from the tropical storm stage), the results show that there is still a clear tendency of the inner-core tangential winds to exceed the gradient wind values near the RMW; for one particular sonde inside the RMW, the layer-averaged tangential winds exceed the gradient wind by nearly 50%. As the storm intensifies, the difference between the layer-averaged tangential wind and gradient wind increases significantly. These features are to be expected if the boundary layer is exerting a progressively stronger control on the vortex circulation (Montgomery and Smith, 2011; Smith *et al.*, 2012). In summary, the layer-averaged results support the original calculations and suggest that the boundary-layer spin-up mechanism, which is responsible for generating the supergradient winds, is active even during the early intensification phase from the tropical storm vortex.

5.2. *Testing Carrier et al.'s prediction for the near-surface wind speed*

The data presented above offer a unique opportunity to determine the actual near-surface wind in terms of the gradient wind, which is the quantity predicted by Emanuel's potential intensity theory for a steady-state hurricane (E86; Emanuel, 1995, 2004; Bister and Emanuel, 1998). The question is: to what extent does Emanuel's potential intensity theory for the gradient wind provide a measure for the total wind speed at the surface? Long ago, Carrier *et al.* (1971) and Carrier (1971) and related investigations by Carrier *et al.* (1994, and references therein) predicted that the *total wind speed* in the boundary layer at any height is approximately equal to the gradient wind at the top of the boundary layer. Of course, according to the standard boundary-layer approximation, the gradient wind is approximately uniform throughout the boundary layer. If true, the Carrier prediction would imply that Emanuel's potential intensity theory would be a good approximation to the near-surface wind, which is the preferred measure of intensity used by hurricane forecasters. Restricting attention to the rapid intensification and mature stages of the hurricane, i.e. Figures 8, 9, 11(d, g), it is evident that the near-surface wind speed at the RMW is approximately 33 and 56 m s^{-1} compared with gradient wind speeds of 30 and 36 m s^{-1}, respectively. Under these conditions, the surface wind speeds are underestimated by 10 and 55%! Although the maximum gradient wind during these times is marginally larger, 33 and 50 m s^{-1}, respectively, these maxima occur at a much larger radius than the maximum tangential wind speed in the observations. Specifically, in the first case, the gradient wind maximum occurs at a radius of 70 km compared with 40 km for the observed tangential wind maximum (Figure 11(d)), while in the second case the gradient wind maximum occurs at 100 km compared with 25 km (Figure 11(g)).

5.3. *Testing other near-surface characteristics of the boundary layer*

The studies by Braun and Tao (2000) and Smith and Thomsen (2010) have elevated awareness of an important problem in the design of deterministic forecast models for hurricane intensity, namely which boundary-layer scheme is most appropriate? They provide estimates also of forecast uncertainty which follow from the uncertainty in not knowing the optimum boundary-layer scheme to use. In an effort to address this issue, Kepert (2012) compared a range of boundary-layer parametrization schemes in the framework of a steady-state boundary-layer model in which the tangential wind speed at the top of the boundary layer is prescribed and assumed to be in gradient wind balance. As a result of his analyses, he argues that boundary-layer schemes

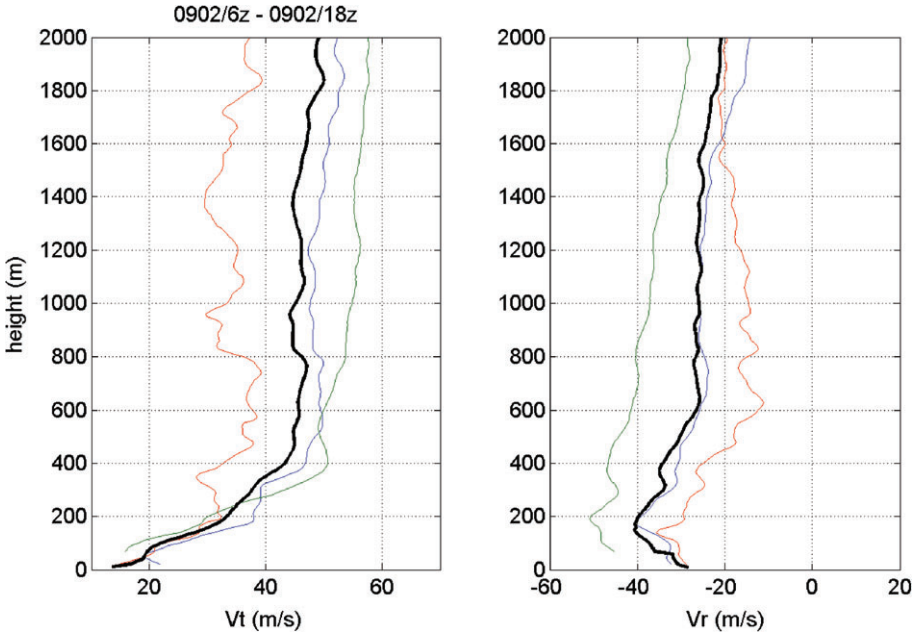

Figure 10. Vertical profiles of storm-relative tangential (V_t) and radial (V_r) wind composites and deviations therefrom in the eyewall region of the vortex during period 4: 0600 to 1800 UTC on 2 September. The eyewall region is defined as the region within 10 km from the RMW deduced using the Dopper radar data. Curves for the same sounding have the same colour. Dark solid curves represent the arithmetic average of dropsonde data within the eyewall region. Maximum V_t is generally located well within the boundary layer, while the maximum V_r is often very close to the surface. The average heights of the maximum tangential wind and maximum inflow during this time are 1800 m and 170 m, respectively, while the average height of the inflow layer is above 2000 m (Table 1).

that do not reproduce a near-surface logarithmic layer are 'badly flawed and should not be used'. However, Smith and Montgomery (2013b) present both observational and theoretical evidence that calls into question the existence of a near-surface logarithmic layer in the inner core of a tropical cyclone.

The observational data presented here offer a new opportunity to assess the foregoing issue in the high-wind region of the storm for both the composite boundary layer and individual vertical profiles. From the data shown, the composite tangential wind component in the boundary layer is a minimum at the surface. While the magnitude of the composite tangential wind generally increases with height near the surface, that of the composite mean radial velocity decreases with height, except in a relatively shallow layer above the sea surface during the intensification and mature stages. Thus, the maximum radial inflow is very close to the sea surface, which is consistent with fluid dynamical considerations for a rapidly rotating vortex adjacent to a frictional boundary (e.g. Bödewadt, 1940; Schlichting, 1968, chapter 11).

The shallow layer of increasing radial inflow is below 50 m during period 1, below 100 m during period 3 and below 200 m during the early weakening stage of period 4. Interestingly, a negative vertical gradient of composite mean radial velocity is evident throughout the boundary layer during period 2. During this period, the maximum mean inflow resides within 50 m from the surface. In those profiles where the radial wind speed increases slightly with height below approximately 100 m, we cannot definitively rule out the existence of a shallow log profile for the composite mean boundary-layer structure. Nevertheless, for reasons given by Smith and Montgomery (2013b), we *can* rule out a strict log layer extending 200 m in depth as proposed by Powell *et al.* (2003) for inferring drag coefficients at major hurricane wind speeds. However, for reasons given in Smith and Montgomery (2013b), the subsequent decrease in the magnitude of the radial wind component above this height is not consistent with a traditional log-layer. The data in Table 3 (last column) show that the percentage of eyewall soundings with a negative vertical gradient of the radial wind magnitude is up to 80% (!), challenging the notion that there is always a shallow log layer in the inner core of a hurricane vortex (cf. Smith and Montgomery, 2013b).

The observational data presented offer also an opportunity to examine the surface inflow angle and to compare these with previous observations and the predictions of different boundary-layer schemes (Smith and Thomsen, 2010). Surface inflow angles derived from recent observational studies of hurricanes *Georges* (1998), *Mitch* (1998), *Danielle* (1998) and *Isabel* (2003) show maximum inflow angles of 24, 18, 24 and 26°, respectively[†]. From their comparison with five different boundary-layer schemes, Smith and Thomsen (2010) found a range of inflow angle values between 17 and 35° depending on the particular boundary-layer scheme. However, from Table 1, the average surface inflow angle in the eyewall region for the different observation periods of *Earl* show surface inflow angles of 12, 35, 46, 57°, for periods 1, 2, 3 and 4, respectively. These values are consistent also with the composite analysis of surface inflow angle presented by Zhang and Uhlhorn (2012). In this respect, these observations suggest that the boundary-layer schemes studied by Smith and Thomsen are within the range of observed variability.

5.4. *Testing gradient wind balance above the boundary layer*

It is widely thought that gradient wind balance holds above the boundary layer (e.g. Willoughby, 1990, 1995). The extensive dropsonde data collected offers an opportunity to test this assumption up to the level of the dropsondes using the same methodology of the foregoing subsection. We have carried out these calculations for the height level of 2 km. This altitude is below the altitude of release for all sondes, but still above the strong inflow layer associated with surface friction, so it may be plausibly considered part of the low-level vortex interior. The results are summarized in Figure 12(a, c) (for period 1), 12(b, d) (for period 2), 12(e, g) (for period 3) and 12(f, h) (for period 4), respectively. In broad terms, there is a clear tendency for the tangential winds near and inside the RMW to exceed the gradient wind even at this altitude. For the period commencing with tropical storm strength winds (period 1), there is again a modest, but clear tendency for the inner-core winds to exceed the gradient wind values near and inside the RMW. For one particular

[†]The first of these angles is based on the right panels of the first and third rows of Figure 9 in Kepert (2006a), the second on panels (b) and (d) of Figure 6 in Kepert (2006b), the third from the second panels of each column of Figure 4 in Schwendike and Kepert (2008) and the fourth on the two right panels of Figure 19 in the same article.

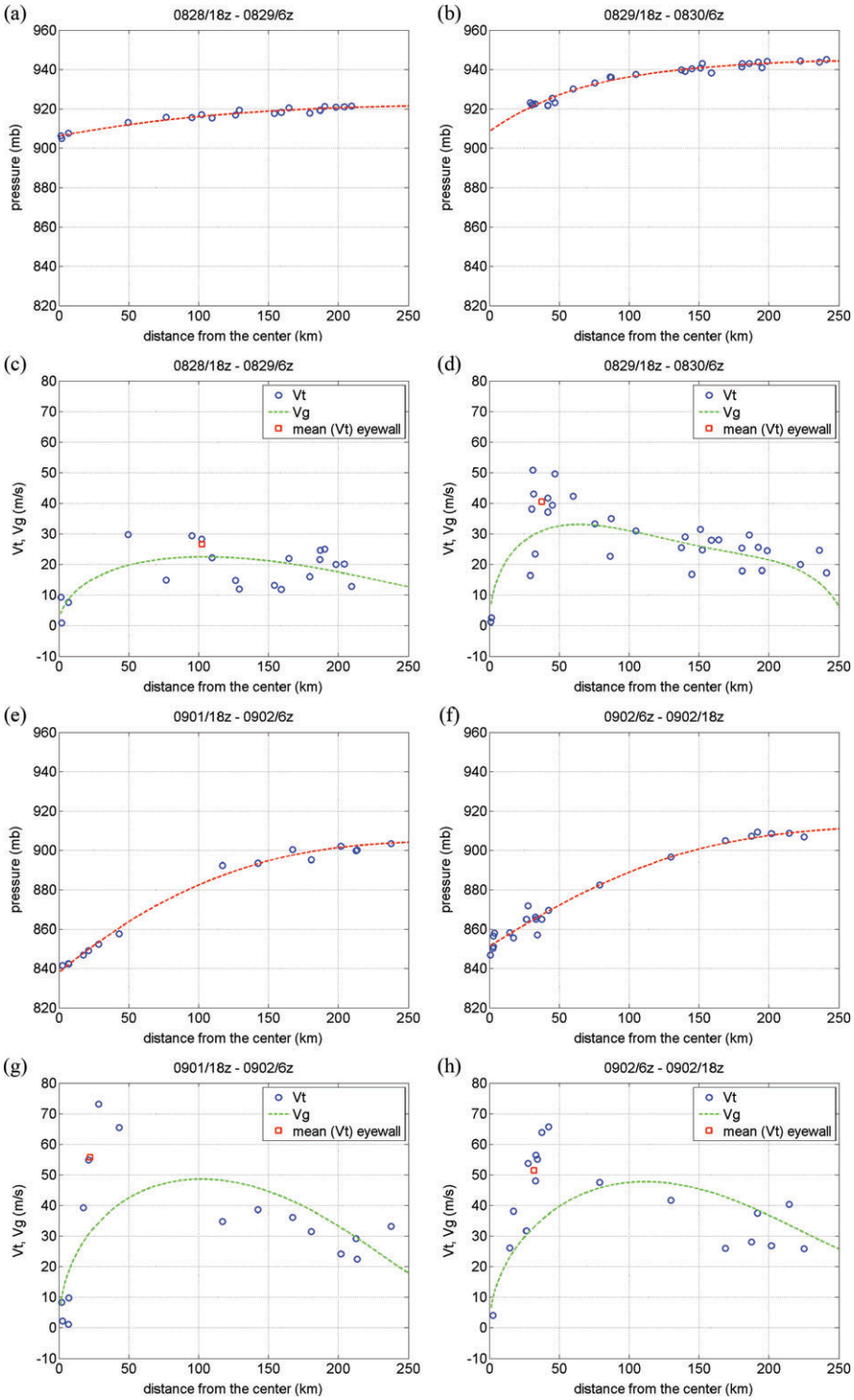

Figure 11. Gradient wind calculation at the height of maximum tangential wind speed (V_t) for periods 1–4 (28 August, 29 August, 1 September and 2 September; Table 1 gives further details). Calculations are displayed in pairs with dropsonde-observed pressure at the top and dropsonde-observed V_t at the bottom of each plotted pair. For each pair, the top panel shows dropsonde pressure observations (blue) as a function of radius with the fitted curve (red) based on least-squares regression. Bottom panels show dropsonde observed V_t (blue) and gradient wind V_g (green) as a function of radius. V_g is calculated using the pressure gradient by solving the gradient balance equation. The red square in the V_t plot is the arithmetic average of V_t at the eyewall region within 5 km on either side of the RMW at 2 km altitude inferred from the Doppler radar data.

Table 3. Summary of boundary-layer parameters for the eyewall region (within 10 km from the RMW) for periods 1, 2, 3 and 4 investigated in this study.

Period	Average height of $V_{t\max}$ (m)	Average height of inflow layer (m)	Average height of peak inflow (m)	Average near-surface inflow angle (deg)	Percent negative $\partial\lvert V_r\rvert/\partial z$ (%)
1	700	700	180	12	25
2	570	1500	50	35	80
3	540	1800	10	46	50
4	800	> 2000	190	57	15

The average height of the inflow layer is defined nominally (following Zhang *et al.*, 2011) as the height of 10% of the peak inflow. The inflow angle is $\tan^{-1}(-u/v)$ averaged over the lowest 50 m. The final column shows %age of data where $\partial\lvert V_r\rvert/\partial z$ is negative below 200 m.

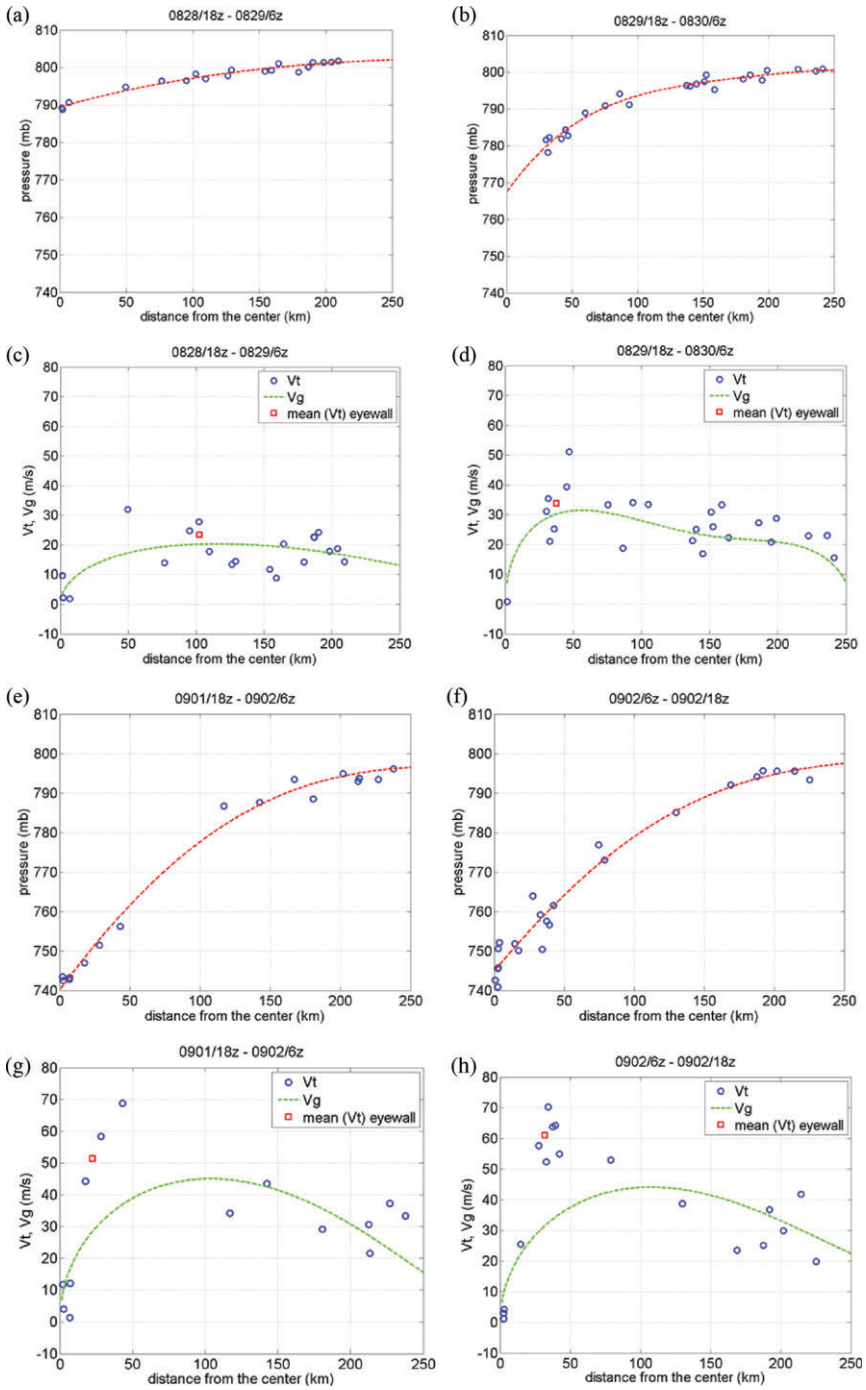

Figure 12. Comparison between gradient wind V_g and tangential speed V_t at height 2 km for observation periods 1–4 (Table 1 gives details). Calculations are displayed in pairs with dropsonde-observed pressure at the top and dropsonde-observed V_t and V_g at the bottom of each plotted pair. For each pair, the top panel shows dropsonde pressure observations (blue) as a function of radius with the fitted curve (red) based on least-squares regression. Bottom panels show dropsonde observed V_t (blue) and gradient wind V_g (green) as a function of radius. V_g is calculated as in Figure 11. The red square in the V_t plot is the arithmetic average of V_t at the eyewall region within 5 km on either side of the RMW at 2 km altitude inferred from the Doppler radar data.

sonde inside the RMW, the tangential winds exceed the gradient wind by nearly 50% at this altitude above the strong inflow layer. From the other figures, it is evident also that, as the storm intensifies, the difference between the gradient and tangential wind increases significantly with storm intensity above the strong inflow layer. These results differ from those of Willoughby (1990) who concluded using flight-level data that the flow above the frictional boundary layer (above the level corresponding to 850 hPa) is very close (less than 1.5 m s^{-1}, with no bias) to gradient wind balance. These results support the argument summarized in the Introduction that the boundary-layer spin-up mechanism contributes to the amplification of the interior tangential wind field by lofting air with high tangential momentum from the boundary layer. Echoing our remarks above, these features are to be expected if the boundary layer is exerting a progressively stronger control on the vortex circulation (Montgomery and Smith, 2011; Smith *et al.*, 2013). In summary, the results suggest that the gradient wind balance approximation above the strong inflow layer may not be as accurate as has been widely held in the inner-core region of a tropical cyclone during its intensification.

5.5. *Thermodynamic structure in the boundary layer*

As discussed in the Introduction, it is desired to learn more about the thermodynamics of the boundary layer and lower troposphere during the intensification process. In previous work we examined the inner-core and outer-core thermodynamic structure by simply binning the data into two radial groups, the eyewall region and the outer core region (Smith and Montgomery, 2013a). We use now the data to construct radial profiles of boundary layer θ_e at both the 100 and 1500 m levels. θ_e was calculated according to Bolton (1980). The results are shown in Figure 13 for three

separate periods. At both levels, the increase of θ_e with decreasing radius is approximately monotonic within 150 km radius. The radial gradient of θ_e is relatively weak during the intensification phase, but becomes quite pronounced during the mature phase of the vortex evolution. At both levels, the difference between θ_e at the axis and 150 km radius increases from about 5 to 20 K over the observation period.

Montgomery *et al.* (2009) and Montgomery and Smith (2013) noted that a radial increase in near-surface θ_e with decreasing radius is necessary to maintain a degree of convective instability in the inner-core region of a tropical cyclone in the presence of a developing warm core aloft during intensification. Early in the intensification period of hurricane *Earl*, the difference in θ_e between the heights 100 and 1500 m is approximately 10 K beyond 150 km radius and this difference decreases to 8 K as the radius decreases to 50 km near the nascent eyewall. During the rapid intensification and mature period, the difference in θ_e between the heights 100 and 1500 m is approximately 12 K beyond 150 km radius and this difference decreases to 5 K as one moves inwards to the RMW near the 25 km radius. During the re-intensification period after the eyewall replacement cycle, the difference is somewhat smaller, though the absence of data in this intermediate region cautions us against making quantitative statements.

These observations provide support for a similar finding in high-resolution numerical simulations. In both observations and model, the lack of vertical mixing may be attributable to the large vertical shear in both the tangential and radial winds near the surface. As an illustration, we present in Figure 14 an example from a high-resolution numerical simulation of an intensifying tropical cyclone. The simulation is taken from Smith and Thomsen (2010) using the Blackadar boundary-layer scheme (all other boundary-layer schemes yield similar results – not shown). Figure 14 shows an azimuthally averaged radius–height plot of θ_e that looks very similar to the observations shown in Figure 13. Specifically, Figure 14 shows the azimuthally averaged vertical velocity, radial velocity and corresponding θ_e field. The mean pattern of the vertical velocity field is completely accounted for, yet the radius–height θ_e structure in the lowest levels is remarkably similar to Figure 13. These numerical results suggest that the azimuthally averaged boundary-layer θ_e is not well-mixed for several hundred kilometres from the centre of the vortex. This finding is contrary to the well-mixed assumption for θ_e invoked in axisymmetric theoretical formulations of the hurricane boundary layer (e.g. Emanuel 1986, 1988, 1989, 1995, 1997, 2003, 2012; Bryan and Rotunno, 2009). Here we propose an analogy with the 'shear sheltering' concept that has been proffered to explain 'anti-mixing' in strongly sheared boundary-layer flows (e.g. Hunt and Durbin, 1999; Smedman *et al.*, 2004) and also in part 'eddy transport barriers' (e.g. Dritschel and McIntyre, 2008, and references therein), and hypothesize that the strong vertical shear of the tangential and radial winds in the vortex boundary layer plays an important role in limiting vertical mixing of θ_e in the boundary layer across the broad scale of the hurricane vortex.

In summary, the axisymmetric θ_e structure inferred from the observations at 1.5 km altitude is consistently less than the corresponding near-surface value at all radii, even where the air is ascending into the eyewall. In the innermost 150 km, the maximum difference is approximately 10 K, while the minimum is about 5 K. These observations suggest that the air going up into the eyewall has significantly lower values of θ_e than those near the surface. This finding is not consistent with the axisymmetric eruption of the boundary layer into the eyewall unless there are non-conservative (eddy) processes acting to modify the entropy of ascending air. As an example, as suggested by D. Raymond (personal communication), the expected high values of θ_e at 1.5 km may be concentrated in isolated updraughts that were missed by the dropwindsondes, whereas these θ_e values are more spread out at the surface. If the pilots were deviating around high-reflectivity areas as they penetrated the eyewall, this would almost certainly be the case. These latter considerations implicate

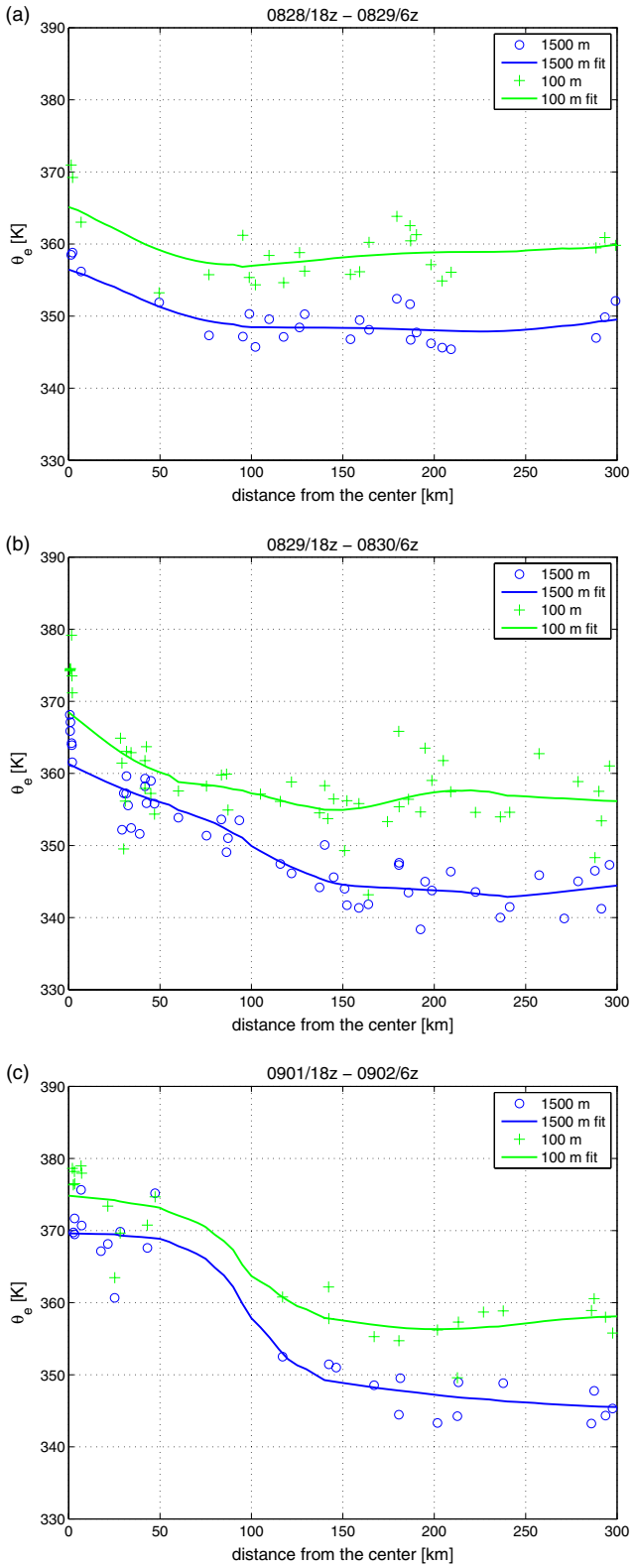

Figure 13. Values of θ_e at heights of 100 and 1500 m as a function of radius, for three 12 h periods. [Correction added ~~12~~ September 2014 after original online publication: in Figure 13 units for the x axis have been corrected to 'km'.]

an important role of localized updraughts and associated eddy processes in the eyewall region during the intensification of a tropical cyclone (Persing *et al.*, 2013).

The ramification of these thermodynamic findings and interpretations remains a topic for future study, but lies outside the scope of this article.

6. Conclusions

We have examined dynamic and thermodynamic aspects of Atlantic hurricane *Earl* (2010) during its intensification and

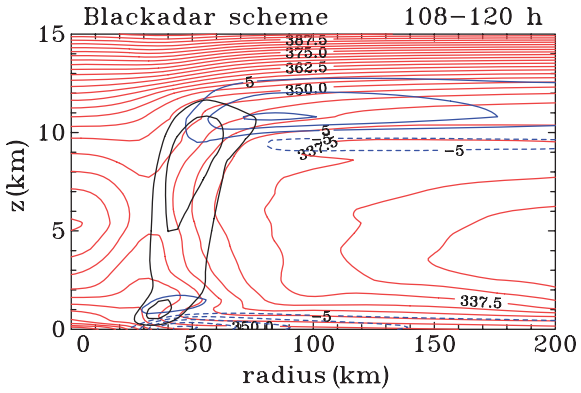

Figure 14. Vertical cross-section of the azimuthally averaged θ_e field taken from the mature stage of the idealized numerical simulation described by Smith and Thomsen (2010) using the Blackadar boundary-layer scheme (red contours, contour interval 2.5 K). Superimposed are the isotachs of azimuthally averaged radial velocity (blue contours, with interval 5 m s^{-1} and negatives dashed) and vertical velocity (black contours, with interval 0.5 m s^{-1}).

mature phases over four days of intensive measurements. The observations are based on a unique dataset comprising airborne Doppler radar and dropwindsondes released from the lower and upper troposphere during the collaborative NASA-GRIP and NOAA-IFEX field studies. These observational resources were supplemented with US Air Force reconnaissance dropwindsonde data. The three (and sometimes four) aircraft that flew in *Earl* collected an observational dataset that is perhaps the most extensive ever for an intensifying and mature hurricane. Here we use these observations to appraise elements of a new model for tropical-cyclone intensification articulated by Montgomery and Smith (2013).

The absolute angular momentum surfaces are shown to move progressively inwards over a deep layer as the storm intensifies. Also, the signature of the strengthening boundary-layer inflow is evident by the increase in the upward-outward tilt of the M surfaces in the lower troposphere as these surfaces move inwards. During spin-up and maturity, the maximum tangential winds persistently occur within the layer of strong boundary-layer inflow ($<$ 1 km depth). The dropsonde composites show that the maximum radial inflow is very close to the sea surface, which is consistent with fluid dynamical considerations for a rapidly rotating vortex adjacent to a frictional boundary.

The tangential winds near the radius of maximum wind in the boundary layer are persistently and significantly supergradient. For brevity, we have shown this only at the height of maximum tangential wind, but supporting analyses over the layer between 400 and 1000 m confirm this tendency throughout much of the boundary layer, except very near the surface where the tangential winds become subgradient. The average maximum tangential winds beneath the eyewall exceed the gradient wind by between 20 and 60%, with the largest excess occurring during the re-intensification period following the eyewall replacement on 2 September. An analysis of the possible departures from gradient wind balance above the boundary layer at 2 km altitude using the same methodology was conducted also. The results suggest that the gradient wind balance approximation in the low-level vortex interior above the strong inflow layer may not be as accurate as has been widely held in the inner-core region of a tropical cyclone during its intensification. As an indication of the inaccuracy of the gradient wind for characterizing the structure of the vortex, the radius of the gradient wind maximum is up to three times the radius of the maximum observed tangential wind speed. At the radius of the observed tangential wind speed maximum, it is found that the maximum averaged surface wind speed is sometimes significantly underestimated by the gradient wind speed.

The near-surface θ_e and that at a height of 1.5 km increase approximately monotonically with decreasing radius within 150 km of the storm axis. The radial gradient of θ_e is relatively weak during the intensification phase, but becomes pronounced during the mature phase of the vortex evolution. Interestingly, the value of θ_e at 1.5 km altitude is consistently less than the corresponding near-surface value at all radii, even where the air is ascending into the eyewall. Specifically, in the innermost 150 km, the maximum difference is approximately 10 K, while the minimum is about 5 K. The results suggest that the azimuthally averaged boundary-layer θ_e is not vertically well-mixed for several hundred kilometres from the centre of the vortex, contrary to the well-mixed assumption for θ_e invoked in theoretical formulations of the hurricane boundary layer. The observations provide support for a similar finding in high-resolution numerical simulations, and support the hypothesis that the lack of vertical mixing of θ_e in nature may be attributable to the large vertical shear in both the tangential and radial winds near the surface.

The axisymmetric vortex structure inferred from the observations suggest that the air going up into the eyewall has significantly lower values of θ_e than those near the surface. This finding is not consistent with the axisymmetric eruption of the boundary layer into the eyewall unless there are non-conservative (eddy) processes acting to modify the entropy of ascending air. These considerations implicate an important role of localized updraughts and associated eddy processes in the eyewall region during the intensification of a tropical cyclone. The ramification of these thermodynamic findings and interpretations remains a topic for future study.

The findings herein complement recent observational work of Sanger *et al.* (~~2013~~) and provide further support for the new paradigm of tropical cyclone intensification.

Acknowledgements

We acknowledge NASA and Ramesh Kakar for their support of the GRIP experiment. MTM acknowledges the support of NSF AGS-0733380 and NASA grants NNH09AK561, NNG11PK021 and NNG09HG031. JAZ acknowledges the support from NOAA's Hurricane Forecast and Improvement Program (HFIP). We want to thank Sim Aberson and Sylvie Lorsolo for providing the radar composite data for each *Earl* flight. JAZ is grateful also to Robert Rogers and Paul Reasor for helpful discussions. Finally, we would like to thank Dave Raymond and Jonathan Vigh for their perceptive and constructive reviews.

References

Bell MM, Montgomery MT. 2008. Observed structure, evolution, and potential intensity of category 5 hurricane *Isabel* (2003) from 12 to 14 September. *Mon. Weather Rev.* **65**: 2025–2046.
Bister M, Emanuel KA. 1998. Dissipative heating and hurricane intensity. *Meteorol. Atmos. Phys.* **65**: 233–240.
Bödewadt UT. 1940. Die Drehströmung über festem Grund. *Z. Angew. Math. Mech.* **20**: 241–253.
Bolton D. 1980. The computation of equivalent potential temperature. *Mon. Weather Rev.* **108**: 1046–1053.
Braun SA, Tao W-K. 2000. Sensitivity of high-resolution simulations of hurricane *Bob* (1991) to planetary boundary-layer parameterizations. *Mon. Weather Rev.* **128**: 3941–3961.
Bryan GH, Rotunno R. 2009. Evaluation of an analytical model for the maximum intensity of tropical cyclones. *J. Atmos. Sci.* **66**: 3042–3060.
Bui HH, Smith RK, Montgomery MT, Peng J. 2009. Balanced and unbalanced aspects of tropical-cyclone intensification. *Q. J. R. Meteorol. Soc.* **135**: 1715–1731.
Carrier GF. 1971. Swirling flow boundary layers. *J. Fluid Mech.* **49**: 133–144.
Carrier GF, Hammond AL, George OD. 1971. A model of the mature hurricane. *J. Fluid Mech.* **47**: 145–170.
Carrier GF, Fendell F, Mitchell J, Bronstein M. 1994. Self-sustaining intense vortices. *Physica D* **77**: 77–96.
Charney JG, Eliassen A. 1964. On the growth of the hurricane depression. *J. Atmos. Sci.* **21**: 68–75.
Dritschel DG, McIntyre ME. 2008. Multiple jets as PV staircases: The Phillips effect and the resilience of eddy-transport barriers. *J. Atmos. Sci.* **65**: 855–874.
Elsberry R, Harr P. 2008. Tropical cyclone structure (TCS08) field experiment scientific basis, observational platforms, and strategy. *Asia-Pac. J. Atmos. Sci.* **44**: 1–23.
Emanuel KA. 1986. An air–sea interaction theory for tropical cyclones. Part I: Steady state maintenance. *J. Atmos. Sci.* **43**: 585–604.

Emanuel KA. 1988. The maximum intensity of hurricanes. *J. Atmos. Sci.* **45**: 1143–1155.

Emanuel KA. 1989. The finite amplitude nature of tropical cyclogenesis. *J. Atmos. Sci.* **46**: 3431–3456.

Emanuel KA. 1994. *Atmospheric Convection*. Oxford University Press: Oxford, UK.

Emanuel KA. 1995. Sensitivity of tropical cyclones to surface exchange coefficients and a revised steady-state model incorporating eye dynamics. *J. Atmos. Sci.* **52**: 3969–3976.

Emanuel KA. 1997. Some aspects of hurricane inner-core dynamics and energetics. *J. Atmos. Sci.* **54**: 1014–1026.

Emanuel KA. 2003. Tropical cyclones. *Annu. Rev. Earth Planet. Sci.* **31**: 75–104.

Emanuel KA. 2004. Tropical cyclone energetics and structure. In *Atmospheric Turbulence and Mesoscale Meteorology*, Fedorovich E, Rotunno R, Stevens B (eds): 280 pp. Cambridge University Press: Cambridge, UK.

Emanuel KA. 2012. Self-stratification of tropical cyclone outflow. Part II: Implications for storm intensification. *J. Atmos. Sci.* **69**: in press.

Emanuel KA, Rotunno R. 2011. Self-stratification of tropical cyclone outflow. Part I: Implications for storm structure. *J. Atmos. Sci.* **68**: 2236–2249.

Emanuel KA, Neelin JD, Bretherton CS. 1994. On large-scale circulations in convecting atmospheres. *Q. J. R. Meteorol. Soc.* **120**: 1111–1143.

Franklin JL, Lord SJ, Feuer SE, Marks FD. 1993. The kinematic structure of hurricane *Gloria* (1985) determined from nested analyses of dropwindsonde and Doppler radar data. *Mon. Weather Rev.* **121**: 2433–2451.

Franklin JL, Black ML, Valde K. 2003. GPS dropwindsonde wind profiles in hurricanes and their operational implications. *Weather and Forecasting* **18**: 32–44.

Gamache JF. 1997. Evaluation of a fully three-dimensional variational Doppler analysis technique. *Preprints, 28th Conference on Radar Meteorology, Austin, TX*. 422–423. American Meteorological Society: Boston, MA.

Gamache JF. 2012. 'Real-time dissemination of hurricane wind fields determined from airborne doppler radar data.' National Hurricane Center: Miami, FL. http://www.nhc.noaa.gov/jht/2003-2005reports/DOPLRgamache_JHTfinalreport.pdf (accessed 15 November2013).

Hawkins HF, Imbembo SM. 1976. The structure of a small, intense hurricane *Inez* (1966). *Mon. Weather Rev.* **104**: 418–442.

Hock TF, Franklin JL. 1999. The NCAR GPS dropwindsonde. *Bull. Am. Meteorol. Soc.* **80**: 407–420.

Hunt JCR, Durbin PA. 1999. Perturbed vortical layers and shear sheltering. *Fluid Dyn. Res.* **24**: 375–404.

Kepert JD. 2006a. Observed boundary-layer wind structure and balance in the hurricane core. Part I. Hurricane *Georges*. *J. Atmos. Sci.* **63**: 2169–2193.

Kepert JD. 2006b. Observed boundary-layer wind structure and balance in the hurricane core. Part II. Hurricane *Mitch*. *J. Atmos. Sci.* **63**: 2194–2211.

Kepert JD. 2012. Choosing a boundary-layer parameterisation for tropical cyclone modelling. *Mon. Weather Rev.* **140**: 1427–1445.

Marks F, Houze RA, Gamache JF. 1992. Dual-aircraft investigation of the inner core of hurricane *Norbert*. Part I: Kinematic structure. *J. Atmos. Sci.* **49**: 919–942.

Marks FD, Black PG, Montgomery MT, Burpee RW. 2008. Structure of the eye and eyewall of hurricane *Hugo* (1989). *Mon. Weather Rev.* **136**: 1237–1259.

Montgomery MT, Smith RK. 2011. Tropical cyclone formation: Theory and idealized modelling. *Proceedings of Seventh WMO International Workshop on Tropical Cyclones (IWTC-VII)*, La Réunion, November 2010. (WWRP 2011–1). World Meteorological Organization: Geneva, Switzerland.

Montgomery MT, Smith RK. 2013. Paradigms for tropical-cyclone intensification. *Aust. Meteorol. Oceanogr. J.* in press; 2.1.1-2.1.23. http://www.wmo.int/pages/prog/arep/wwrp/tmr/otherfileformats/documents/2_1.pdf.

Montgomery MT, Bell MM, Aberson SD, Black ML. 2006. Hurricane *Isabel* (2003): New insights into the physics of intense storms. Part I. Mean vortex structure and maximum intensity estimates. *Bull. Am. Meteorol. Soc.* **87**: 1335–1347.

Montgomery MT, Nguyen SV, Smith RK, Persing J. 2009. Do tropical cyclones intensify by WISHE? *Q. J. R. Meteorol. Soc.* **135**: 1697–1714.

Nguyen SV, Smith RK, Montgomery MT. 2008. Tropical-cyclone intensification and predictability in three dimensions. *Q. J. R. Meteorol. Soc.* **134**: 563–582.

Ooyama KV. 1964. A dynamical model for the study of tropical cyclone development. *Geophys. Int.* **4**: 187–198.

Ooyama KV. 1969. Numerical simulation of the life cycle of tropical cyclones. *J. Atmos. Sci.* **26**: 3–40.

Ooyama KV. 1982. Conceptual evolution of the theory and modeling of the tropical cyclone. *J. Meteorol. Soc. Japan* **60**: 369–380.

Persing J, Montgomery MT, McWilliams JC, Smith RK. 2013. Asymmetric and axisymmetric tropical cyclone dynamics. *Atmos. Chem. Phys.* **13**: 12299–12341.

Powell MD, Vickery PJ, Reinhold TA. 2003. Reduced drag coefficient for high wind speeds in tropical cyclones. *Nature* **422**: 279–283.

Reasor PD, Eastin MD. 2012. Rapidly intensifying hurricane *Guillermo* (1997). Part II: Resilience in shear. *Mon. Weather Rev.* **140**: 425–444.

Reasor PD, Eastin M, Gamache JF. 2009. Rapidly intensifying hurricane *Guillermo* (1997). Part I: Low-wavenumber structure and evolution. *Mon. Weather Rev.* **137**: 603–631.

Reasor PD, Rogers D, Lorsolo S. 2013. Environmental flow impacts on tropical cyclone structure diagnosed from airborne Doppler radar composites. *Mon. Weather Rev.* **141**: 2949–2969.

Sanger NT. 2011. 'An observational study of tropical cyclone spinup in supertyphoon *Jangmi* and hurricane *Georges*', PhD dissertation. US Naval Postgraduate School: Monterey, CA.

Sanger NT, Montgomery MT, Smith RK, Bell MM. ~~2013~~ An observational study of tropical-cyclone spin-up in supertyphoon *Jangmi* from 24 to 27 September. *Mon. Weather Rev.* ~~In press, doi: 10.1175/MWR-D-12-00306.1.~~

Schlichting H. 1968. *Boundary-Layer Theory* (6th edn). McGraw-Hill: New York, NY.

Schwendike J, Kepert JD. 2008. The boundary-layer winds in hurricane *Danielle* (1998) and hurricane *Isabel* (2003). *Mon. Weather Rev.* **136**: 3168–3192.

Shapiro LJ, Montgomery MT. 1993. A three-dimensional balance theory for rapidly-rotating vortices. *J. Atmos. Sci.* **50**: 3322–3335.

Smedman A-S, Högström U, Hunt JCR. 2004. Effects of shear sheltering in a stable atmospheric boundary layer with strong shear. *Q. J. R. Meteorol. Soc.* **130**: 31–50.

Smith RK, Montgomery MT. 2010. Hurricane boundary-layer theory. *Q. J. R. Meteorol. Soc.* **136**: 1665–1670.

Smith RK, Montgomery MT. 2013a. How important is the isothermal expansion effect in elevating equivalent potential temperature in the hurricane inner core? *Q. J. R. Meteorol. Soc.* **139**: 70–74.

Smith RK, Montgomery MT. 2013b. On the existence of the logarithmic surface layer in hurricanes. *Q. J. R. Meteorol. Soc.*

Smith RK, Thomsen GL. 2010. Dependence of tropical-cyclone intensification on the boundary-layer representation in a numerical model. *Q. J. R. Meteorol. Soc.* **136**: 1671–1685.

Smith RK, Montgomery MT, Vogl S. 2008. A critique of Emanuel's hurricane model and potential intensity theory. *Q. J. R. Meteorol. Soc.* **134**: 551–561.

Smith RK, Montgomery MT, Nguyen SV. 2009. Tropical-cyclone spin up revisited. *Q. J. R. Meteorol. Soc.* **135**: 1321–1335.

Willoughby HE. 1988. The dynamics of the tropical cyclone core. *Aust. Meteorol. Mag.* **36**: 183–191.

Willoughby HE. 1990. Gradient balance in tropical cyclones. *J. Atmos. Sci.* **47**: 465–489.

Willoughby HE. 1995. Mature structure and evolution. In *Global Perspectives on Tropical Cyclones*, WMO/TD-No 693, Elsberry RL. (ed.): 21–62. World Meteorological Organization: Geneva, Switzerland.

Willoughby HE, Chelmow M. 1982. Objective determination of hurricane tracks from aircraft observations. *Mon. Weather Rev.* **110**: 198–1305.

Zhang JA, Uhlhorn EW. 2012. Hurricane sea-surface inflow angle and an observation-based parametric model of the two-dimensional surface wind field. *Mon. Weather Rev.* **140**: 3587–3604.

Zhang D-L, Liu Y, Yau MK. 2001. A multi-scale numerical study of hurricane *Andrew* (1992). Part IV: Unbalanced flows. *Mon. Weather Rev.* **129**: 92–107.

Zhang JA, Drennan WM, Black PG, French JR. 2009. Turbulence structure of the hurricane boundary layer between the outer rainbands. *J. Atmos. Sci.* **66**: 2455–2467.

Zhang JA, Rogers RF, Nolan DS, Marks FD. 2011. On the characteristic height scales of the hurricane boundary layer. *Mon. Weather Rev.* **139**: 2523–2535.

